EDGE ARTICLE

Check for updates

A homoleptic alkynyl-protected [Ag$_9$Cu$_6$(^{t}BuC≡C)$_{12}$]$^+$ superatom with free electrons: synthesis, structure analysis, and different properties compared with the Au$_7$Ag$_8$ cluster in the M$_{15}$$^+$ series†

Xiaoshuang Ma,‡[a] Lin Xiong,‡[b] Lubing Qin,[a] Yun Tang,[a] Guanyu Ma,[a] Yong Pei[*b] and Zhenghua Tang [ID] [*a]

We report the first homoleptic alkynyl-protected AgCu superatomic nanocluster [Ag$_9$Cu$_6$(^{t}BuC≡C)$_{12}$]$^+$ (NC **1**, also Ag$_9$Cu$_6$ in short), which has a body-centered-cubic structure with a Ag$_1$@Ag$_8$@Cu$_6$ metal core. Such a configuration is reminiscent of the reported AuAg bimetallic nanocluster [Au$_1$@Ag$_8$@Au$_6$(^{t}BuC≡C)$_{12}$]$^+$ (NC **2**, also Au$_7$Ag$_8$ in short), which is also synthesized by an anti-galvanic reaction (AGR) approach with a very high yield for the first time in this study. Despite a similar Ag$_8$ cube for both NCs, structural anatomy reveals that there are some subtle differences between NCs **1** and **2**. Such differences, plus the different M$_1$ kernel and M$_6$ octahedron, lead to significantly different optical absorbance features for NCs **1** and **2**. Density functional theory calculations revealed the LUMO and HOMO energy levels of NCs **1** and **2**, where the characteristic absorbance peaks can be correlated with the discrete molecular orbital transitions. Finally, the stability of NCs **1** and **2** at different temperatures, in the presence of an oxidant or Lewis base, was investigated. This study not only enriches the M$_{15}$$^+$ series, but also sets an example for correlating the structure–property relationship in alkynyl-protected bimetallic superatomic clusters.

Introduction

Superatomic coinage bimetallic nanoclusters (NCs) with atomic precision are currently being extensively investigated due to their tunable structure,[1,2] enhanced stability,[3–5] and significantly modified physicochemical properties,[6–8] compared with homonuclear parent clusters.[9–13] Among these monolayer-protected clusters, the most studied combination is Au–Ag, as they are fully miscible in bulk.[14,15] It is well known that a plethora of stable Au NCs have been synthesized and characterized in the past few decades,[16,17] yet stable Ag NCs comprise a rather recent entry in the coinage metal NC field.[18,19] In

[a]Guangzhou Key Laboratory for Surface Chemistry of Energy Materials, New Energy Research Institute, School of Environment and Energy, South China University of Technology, Guangzhou Higher Education Mega Centre, Guangzhou, Guangdong, 510006, P. R. China. E-mail: zhht@scut.edu.cn

[b]Department of Chemistry, Key Laboratory of Environmentally Friendly Chemistry and Applications of Ministry of Education, Xiangtan University, Hunan Province, Xiangtan 411105, P. R. China. E-mail: ypei2@xtu.edu.cn

† Electronic supplementary information (ESI) available: Synthesis, characterization, supporting figures and tables. Details and crystal data of Au$_7$Ag$_8$(C≡C^{t}Bu)$_{12}$SbF$_6$ and Ag$_9$Cu$_6$(C≡C^{t}Bu)$_{12}$SbF$_6$ (cif). CCDC 2072510 and 2072663. For ESI and crystallographic data in CIF or other electronic format see DOI: 10.1039/d1sc03679c

‡ X. Ma and L. Xiong contributed equally to this work.

contrast to Au or Ag, they are far fewer examples of Cu-containing coinage alloy NCs, particularly AgCu molecules. As for the capping agent for protection, mixed ligands can yield a more complicated structure and hence obscure the structure–property relationship establishment; therefore, molecules of single structure type particularly thiolate compounds have been widely employed to prepare AgCu NCs. For instance, in 2016, Zheng's group reported the first thiolated chiral three-concentric-shell cluster containing free valence electrons, [Ag$_{28}$Cu$_{12}$(SR)$_{24}$]$^{4-}$ (SR = 2,4-dichlorobenzenethiolate).[20] In 2018, Zhu's group showcased the controllable synthesis of the AgCu bimetallic NC [Ag$_{40.13}$Cu$_{13.87}$S$_{19}$(^{t}BuS)$_{20}$(^{t}BuSO$_3$)$_{12}$], which consisted of a Cu$_{10}$Ag$_2$S$_7$ core, a M$_{42}$(^{t}BuS)$_{20}$(^{t}BuSO$_3$)$_{12}$ shell, and another 12 bare S atoms.[21] Recently, Bao *et al.* prepared the [Ag$_{13}$Cu$_{10}$(SAdm)$_{12}$]$^{3+}$ (Adm = –SC$_{10}$H$_{15}$) NC, which has a Ag$_{13}$ core and a Cu$_{10}$(SAdm)$_{12}$ shell.[22]

Recently, alkynyl molecules have been emerging as a new type of ligand for preparing coinage metal NCs,[23,24] mainly because alkynyl molecules can generate more diverse surface binding moieties and some undiscovered molecular clusters with magic numbers,[25–30] eventually leading to drastically different functionalities.[31–33] In terms of AuAg NCs, Wang and Zheng groups documented the fabrication of the Au$_{34}$Ag$_{28}$(PhC≡C)$_{34}$ NC and its use as a model catalyst to explore the significance of surface ligands in promoting catalysis.[34] In

another report, Wang *et al.* discovered that when incorporating alkali metal ions or copper atoms into the alkynyl-protected body-centered cubic (BCC) $[Au_7Ag_8(^tBuC≡C)_{12}]^+$ NC (which is also NC **2** in this study), site preference can be observed.[35] Recently, Yuan *et al.* found that the alkynyl-protected monomeric (AuAg)$_{34}$ can be assembled into 1D polymers with Ag–Au–Ag bonds between neighboring clusters through a solvent-mediated approach.[36] In the AgCu regime, the alkynyl ligand has also been utilized. For instance, Williams and co-workers reported two halide-ion-templated heterometallic Ag_8Cu_6 rhombic dodecahedron clusters and investigated the spectroscopic properties and reactivity of these clusters along with those of the parent Ag_{14} NCs.[37] Mak's group employed the designed tetranuclear precursors $[(R–C≡C–C≡C)Ag]_4$ (R = ^iPr, ^tBu, and Ch) to construct a series of heteropolynuclear silver(I)–copper(I) diynyl complexes that bear a common trigonal-planar $CuAg_3$ NC core, and such complexes exhibited long-lived emission upon photoexcitation in various media at room temperature and 77 K.[38] In a recent study, Zang's group discovered that the *o*-carboranealkynyl-protected $[Cu_6Ag_8(C_4-B_{10}H_{11})_{12}Cl]NO_3$ NC can serve as a perfect hypergolic material, as its ignition delay time can be shortened to 15 ms.[39] However, in the above examples of AgCu NCs, all the Ag and Cu atoms are present as the +1 charge state, and no free electrons exist in these clusters. According to the superatom theory,[40] these molecules are regarded as M(I) clusters or complexes rather than superatoms with free electrons. Due to the presence of free electrons, the superatoms have quite different structures and physicochemical properties, and hence they can find different applications in catalysis,[41,42] optoelectronic devices,[36] biomedical regimes[31] and so on. To the best of our knowledge, no case of a homoleptic alkynyl-protected superatomic AgCu NC with free electrons has been reported so far.

Herein, we report the first case of a homoleptic alkynyl-protected AgCu superatomic NC, namely $[Ag_9Cu_6(^tBuC≡C)_{12}]^+$ (NC **1**, also Ag_9Cu_6 in short), which has a BCC-based structure with a three-layered $Ag_1@Ag_8@Cu_6$ metal core configuration. Such a structure is reminiscent of the reported $[Au_7Ag_8(^tBuC≡C)_{12}]^+$ (NC **2**, also Au_7Ag_8 in short) molecule with a $Au_1@Ag_8@Ag_6$ metal architecture, and it is first-time synthesized by an anti-galvanic reaction (AGR) approach with a ultra-high yield in this study. The structural differences between NC **1** and NC **2** result in significantly different optical absorption properties. Comprehensive DFT calculations disclosed the discrete LUMO and HOMO energy levels of NCs **1** and **2**, where the characteristic absorbance peaks of NCs **1** and **2** can be correlated to the specific molecular orbital transitions. Finally, the stability of NCs **1** and **2** at room temperature and 60 °C, in the presence of H_2O_2 or CH_3ONa, was investigated and compared.

Results and discussion

NC **1** was first prepared by following a modified "Two-in-One" method (see experimental details in the ESI†).[43] Briefly, in the presence of $NaSbF_6$, $^tBuC≡CAg(I)$ is reduced by $(PPh_3)_2CuBH_4$ in the mixed solvent of dichloromethane and acetonitrile. The

reaction was aged for 12 h during which the solution gradually changed from colorless to yellow, and finally to dark blue. A blue block crystal was obtained by diffusing methanol into the dichloromethane solution containing the crude product. It is worth noting that by introducing one metal in the precursor and another metal in the reducing agent, such a "Two-in-One" method might be universal for synthesizing bimetallic NCs. NC **2** was synthesized by the AGR approach between organometallic $^tBuC≡CAg(I)$ and $Au_{22}(^tBuC≡C)_{18}$ NC under mild conditions. The synthetic protocols regarding the $^tBuC≡CAg(I)$ precursor and $Au_{22}(^tBuC≡C)_{18}$ can be found in the ESI.†

The chemical compositions of NCs **1** and **2** were verified by electrospray ionization mass spectrometry (ESI-MS) in positive mode. As shown in Fig. 1, the main peak appears at $m/z = 2325.5677$ for NC **1** and 3214.8510 for NC **2**, corresponding well with $[Ag_9Cu_6(C_6H_9)_{12}]^+$ (cal. MW: 2323.5674 Da, deviation: 0.0003 Da) and $[Au_7Ag_8(C_6H_9)_{12}]^+$ (cal. MW: 3214.8515 Da, deviation: 0.0005 Da), respectively. Also, the isotopic distributions of the two NCs match perfectly with the simulated results (inset in Fig. 1A and B). One may notice that there are some fragments in the ESI-MS spectra of NC **1**, and the peak analysis in Fig. S1† shows that the three peaks at $m/z = 2254.6932$, 2299.0153, and 2370.0681 Da can be assigned to $[Ag_7Cu_7(C_6H_9)_{13}]^+$, $[Ag_8Cu_6(C_6H_9)_{13}]^+$, and $[Ag_{10}Cu_5(C_6H_9)_{12}]^+$, respectively. For NC **2**, there is a much less pronounced peak, and the peak assignment analysis in Fig. S2† shows that it can be assigned to $[Au_7Ag_8(^tBuC≡C)_{10}]^+$, which is probably generated by losing two ligands ($–^tBuC≡C$) from parent NC **2**.

Moreover, the fingerprint absorbance peaks of NC **1** are located at 544, 579, and 620 nm, and its characteristic absorbance feature along with the simulated pattern will be discussed next. Nevertheless, we monitored the absorbance change during the formation of NC **1**. As shown in Fig. S3A,† upon reduction, an absorbance peak at 477 nm gradually appeared with the maximal value reached at 1 h. After that, such an absorbance peak gradually diminished and the characteristic peak at 579 nm from NC **1** gradually emerged. The 477 nm absorbance peak indicates that some intermediate may exist; however, several attempts to isolate it were not successful. As depicted in Fig. S3B,† the sharp color transition from yellow to dark yellow, slight pink and eventually blue can be clearly visualized. To better understand the AGR process from $Au_{22}(^tBuC≡C)_{18}$ to NC **2**, the reaction process was also monitored using time-resolved UV-visible absorption spectra. As shown in Fig. S4A,† the absorbance features of Au_{22} NC disappeared
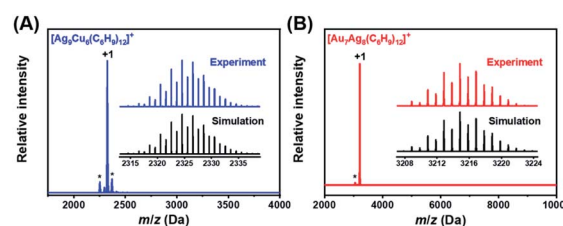

Fig. 1 ESI-MS spectra of NCs **1** (A) and **2** (B) in positive mode. Inset: the experimental isotropic pattern (blue for **1**, and red for **2**) and simulated (black) data of NCs **1** and **2**.

immediately upon the addition of $^tBuC{\equiv}CAg(I)$, while a new absorption band at ∼537 nm emerged. There are two obvious color changes at the time point of $^tBuC{\equiv}CAg(I)$ addition and in the period from 4 to 8 h (Fig. S4B†). After 2 h, the characteristic peak at 487 nm of NC **2** gradually emerged, meanwhile the absorbance peak at 537 nm gradually diminished. It has been postulated but not ascertained that there might be some critical intermediate during the AGR process, which is still under investigation.

The electronic structures of NCs **1** and **2** were subsequently probed by X-ray photoelectron spectroscopy (XPS), and the results are presented in Fig. S5, S6 and Table S1.† As depicted in Fig. S5A,† the XPS survey scan profile confirmed the co-existence of Ag and Cu elements. The Ag/Cu atomic ratio is estimated as 10.33/6.90, in good agreement with the theoretical value (9/6). It can be noted that the binding energy of the Ag $3d_{5/2}$ electrons is located at 368.41 eV, higher than that of bulk Ag (367.9 eV) and lower than that of Ag(I) (368.87 eV) (Fig. S5B†).[44] It suggests that the valence state of Ag in NC **1** is between 0 and +1. Meanwhile, the binding energy of Cu $2p_{3/2}$ (933.12 eV) agrees well with that of Cu(I) (932.45–933.48 eV), implying that six Cu atoms are present as Cu(I) (Fig. S5C†).[45,46] For NC **2**, from the XPS survey scan profile (Fig. S6A†), the Ag/Au atomic ratio can be estimated as 8.27/7.28, in good agreement with the theoretical value (8/7). As shown in Fig. S6B,† the binding energy of the Au $4f_{7/2}$ electrons is located at 84.50 eV, in between those of bulk Au (84.0 eV) and Au(I) (86.0 eV),[47] suggesting that the M_1 core in NC **2** is Au(0). In addition, the binding energy of the Ag $3d_{5/2}$ electrons is located at 368.83 eV, indicating that the valence state of Ag in NC **2** is +1 (Fig. S6C†).[45]

Subsequently, the atomic packing structure of NC **1** was examined using a single-crystal X-ray diffractometer. As illustrated in Fig. S7,† NC **1** crystallizes in the space group $R\bar{3}$, and each unit cell has a SbF_6^- counterion, indicating that NC **1** possessed a +1 charge state. More detailed structural parameters are summarized in Table S2.† The structural anatomy of NC **1** is shown in Fig. 2A, which contains nine silver atoms, six copper atoms and twelve *tert*-butylacetylene ligands, and hence the molecule can be formulated as $[Ag_9Cu_6(^tBuC{\equiv}C)_{12}]SbF_6$. The six copper atoms and twelve alkynyl ligands form six $^tBuC{\equiv}C{-}Cu{-}C{\equiv}C^tBu$ motifs on the surface of this quasi-spherical structure of NC **1** (Fig. 2B). Interestingly, all *tert*-butylacetylene ligands bind with Cu atoms *via* σ bonding, and with Ag atoms in the π manner (Fig. 2C). Note that such linear motifs were observed for the first time in the alkynyl-protected AgCu bimetallic NCs, even though similar linear motifs have been previously documented in several alkynyl-protected AuAg NCs, including Au_7Ag_8,[35] $Au_{24}Ag_{20}$,[48] $Au_{34}Ag_{28}$,[34] $(AuAg)_{34}$,[36] $Au_{57}Ag_{53}$,[49] and $Au_{80}Ag_{30}$.[50] As illustrated in the space-filling structure (Fig. 2D), six Cu sites and eight Ag sites are exposed, which might serve as open active sites for catalysis. Despite the orientation of the rigid ligand on the surface of NC **1** being similar to that of NC **2**, the exposure extent of Ag atoms in NC **2** is somehow more than that in NC **1** (Fig. S8A and B†). However, for NC **2**, even with the same ligand, it is more expansive, probably owing to the much larger radius of the Au atom (Fig. S8C and D†) than that of the Cu atom.
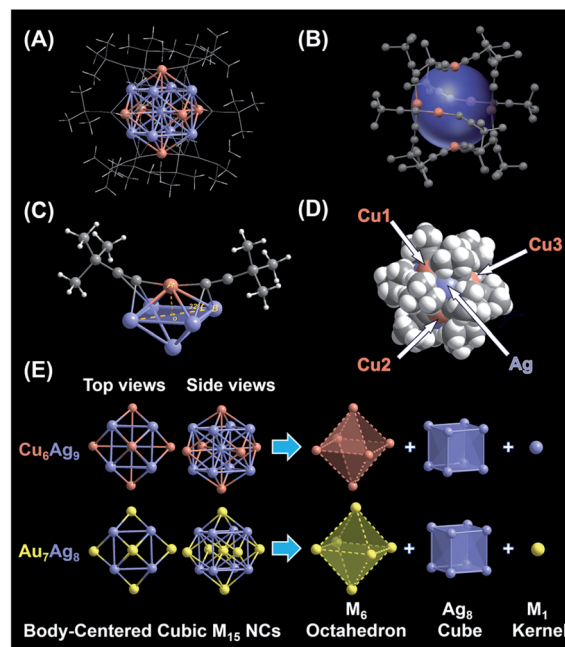

Fig. 2 Structural analysis of body-centered cubic (BCC) M_{15} NCs. (A) Overall structure of monocationic NC **1**. (B) The arrangement of six linear $^tBuC{\equiv}C{-}Cu{-}C{\equiv}C^tBu$ staple motifs on the metal surface. (C) Coordination mode of $^tBuC{\equiv}C{-}$ ligands: μ_2-η^1 (Ag) and η^1 (Cu). (D) The space-filling structure of NC **1**. (E) Anatomy of NCs **1** and **2**. Color legend: Au, yellow; Ag, purple; Cu, orange; C, light gray; hydrogen, white.

Next, the anatomical structure of NC **1** is compared with that of NC **2** (the detailed structural parameters of NC **2** are summarized in Table S3†). As shown in Fig. 2E, NC **1** adopts a core–shell–shell configuration of $Ag_1@Ag_8@Cu_6$, similar to that of NC **2**, as both of them can be classified as the BCC-based M_{15}^+ series with an M_1 kernel@Ag_8 cube@M_6 octahedron architecture. However, the AuAg core in NC **2** is slightly constricted compared to the AgCu core in NC **1**, as the average adjacent Ag–Ag bond length is 3.333 Å and 3.271 Å in the Ag_8 cube for NC **1** and **2**, respectively (Fig. S9†). In addition, the average bond length from the central Ag to the Ag atoms in the Ag_8 cube is 2.887 Å, comparable with that of bulk Ag (2.889 Å). Note that, compared with the reported Ag–Ag bond lengths in alkynyl-protected Ag NCs listed in Table S4,† there is argentophilic Ag–Ag interaction in the Ag@Ag_8 cube for NC **1**. Moreover, as illustrated in Fig. S10A,† the capped Cu atom isn't located exactly above the centre of the Ag_4 plane, which is different from the surface of NC **2** (Fig. S10B†). That means, besides the atom differences in the M_1 kernel and M_6 octahedron, NC **1** and NC **2** have some subtle structural differences, and such subtle differences may affect their physicochemical properties as well. In addition, the structure of the thiolate-protected M_{15} NC $Au_{15}(SR)_{13}$ also has been theoretically proposed, but it is quite different from that of NC **1** and NC **2**, as it consists of a tetrahedral Au_4 core, a $[Au_7(SR)_7]$ ring, and two $[Au_2(SR)_3]$ "staple" motifs.[51]

Next, we first compared the optical absorbance properties of NC **1** and NC **2**. For NC **1**, as shown in Fig. 3A and S11,† there are
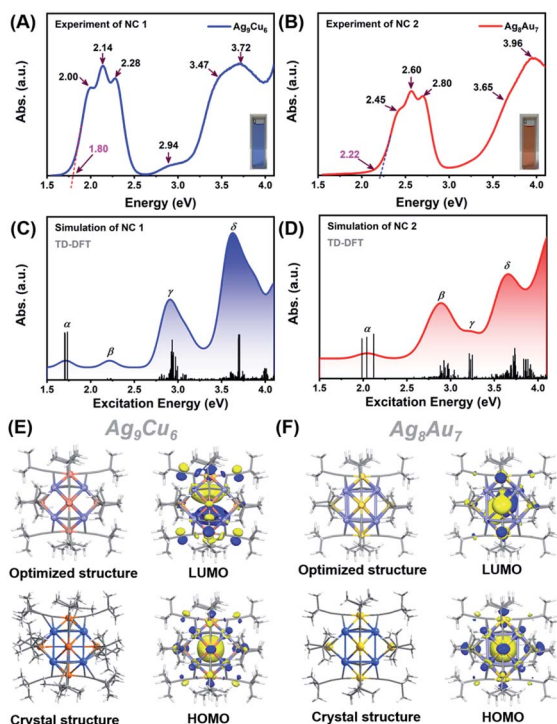
Fig. 3 Experimental absorption spectrum plotted in the energy axis of NCs **1** (A) and **2** (B). Insets show the digital photographs of the NCs in CH_2Cl_2. Simulated absorption spectra of NCs **1** (C) and **2** (D). The electron density diagrams of the HOMO and LUMO orbitals for NCs **1** (E) and **2** (F).

four prominent peaks at 333 nm (3.72 eV), 544 nm (2.28 eV), 579 nm (2.14 eV), and 620 nm (2.00 eV), a broad absorption peak at 422 nm (2.94 eV), and a weak shoulder at 357 nm (3.47 eV). The energy bandgap derived from the absorbance spectrum is ~1.80 eV. For NC **2**, as presented in Fig. 3B and S11,† there are also four prominent peaks at 3.13 nm (3.96 eV), 422 nm (2.80 eV), 477 nm (2.60 eV), and 506 nm (2.45 eV), and a weak shoulder at 339 nm (3.65 eV), while the energy bandgap is ~2.22 eV. It is worth noting that, despite some similar absorbance patterns, the absorbance features are drastically different for NC **1** and NC **2** in terms of the peak position and optical bandgap. Such huge discrepancies can be probably attributed to the structural differences. As both NCs adopt an $M_1@Ag_8@M_6$ metal configuration, the M_1 kernel (Ag vs. Au) can make a dramatically different contribution to the absorbance, and the outer M_6 octahedron (Ag_6 vs. Au_6) not only modulates the geometrical configuration, but also influences the electronic structure (discussed next). Given the standard absorbance curve (Fig. S12A and B†) of the two NCs, according to Lambert–Beer's law, the molecular absorptivity (ε) of NC **1** ($\varepsilon = 0.35 \times 10^4 \ M^{-1} \ cm^{-1}$) and NC **2** ($\varepsilon = 0.78 \times 10^4 \ M^{-1} \ cm^{-1}$) can be determined, as summarized in Table S5.† Therefore, through calculation, the yield of NC **1** was 41.05% (based on Ag, and the yield is 41.74% based on Cu), and the yield of NC **2** was up to 86.72% (based on Au). The details of the calculation process can be found in the ESI† (Fig. S13 and Tables S6, S7†). It is worth noting that the yield of NC **2** here is much higher than that of

the previously reported method. This is mainly due to the fact that the reported method is a "bottom-up" direct reduction approach, in which other polydisperse clusters are also produced, while the AGR method here can yield more homogeneous products, and NC **2** is the main oxidation product (from 4e of Au_{22} NC to 2e of Au_7Ag_8 NC). In addition, we also studied the photo-luminescence properties of the two M_{15} NCs. As shown in Fig. S14,† NC **2** strongly emits in the near-IR region ($\lambda_{max} = 818$ nm), in good agreement with the previous report.[35] However, there is no obvious emission peak for NC **1**.

To elucidate the relationship between the electronic structure and optical properties of NCs **1** and **2**, we carried out time dependent-density functional theory (TD-DFT) calculations. The optimized structure based on the crystal structure is used as a model for TD-DFT calculation. As shown in Fig. 3E and F, there is no change in structure after optimization, except for a slightly distorted orientation of the ligands. The distribution of the electronic cloud map of the highest occupied molecular orbital (HOMO) of NC **1** is quite similar to that of NC **2**, whereas the cloud density position in the lowest unoccupied molecular orbital (LUMO) of NC **1** is quite different from that of NC **2**. From the cloud density distribution, it can be clearly noted that charge transfer occurs from ligands to the metal core for NC **2**, resulting in free electron localization in the metal core. While in stark contrast, charge transfer happens from the metal core to ligands for NC **1**, which leads to a non-radiative loss of excited state electron energy. Such different charge transfer behaviors are probably the main cause of the different luminescence properties. From Fig. 3E, the molecular orbitals of NC **1** revealed a jelliumatic shell closing at the HOMO state of 1S with two electrons and the LUMO state of 1P, in which there was conversion from S to P. It is also in good accord with the electron counting results, as the metal core offers fifteen delocalized electrons; while twelve electrons are delocalized at the metal-core bonds, one electron has to be deducted to form a cation, and hence NC **1** can be literally considered as a two-electron jelliumatic molecule. The absorption feature of NCs **1** and **2** was also theoretically simulated. As shown in Fig. 3C and D, four prominent peaks namely α, β, γ, and δ can be clearly recognized for both NCs, and the detailed transitions corresponding to the significant peaks are listed in Tables S8 and S9† for NCs **1** and **2**, respectively. For NC **1**, an optical bandgap of ca. 1.80 eV is extrapolated according to the value of the absorption edge, which is close to the absorption peak at 1.72 eV (α) in the simulated spectrum. Note that the band α could not be merely considered as a HOMO to LUMO transition, but might be resulted from three transition modes (HOMO to LUMO, HOMO to LUMO + 1, and HOMO to LUMO + 2) with nearly equal contribution values (96.2%, 96.1%, and 95.6%) (Fig. S15A†). Similar transition modes are observed in NC **2** (Fig. 3D and S16A†), and the excitation energy ($\Delta E = 2.04$ eV) is also close to the optical bandgap (exp. 2.22 eV). The β peak at 2.22 eV of NC **1** can also be attributed to three transition modes (HOMO to LUMO + 3, HOMO to LUMO + 4, and HOMO to LUMO + 5), whereas the β peak at 2.89 eV in NC **2** can be assigned to two transition modes (HOMO − 8 to LUMO and HOMO − 8 to LUMO + 1) with the contribution of 42.3% and 12.5%,

respectively (Fig. S15B and S16B†). In addition, the γ peak of NC **1** comprises fifteen transition modes (*e.g.*, HOMO − 6 (67.7%), HOMO − 7 (55.9%), HOMO − 1 (43.5%) to LUMO + 2 and so on) (Fig. S15C†). In contrast, the γ peak of NC **2** can be attributed to six transition modes, including HOMO to LUMO + 4 (69.0%), LUMO + 8 (59.4%), and LUMO + 9 (56.7%) (Fig. S16C†). The δ peak of NC **1** is mainly contributed by the HOMO − 28 to LUMO + 2 (48.2%) transitions (Fig. S15D†), while the δ peak of NC **2** is predominantly contributed by two transition modes (*i.e.*, HOMO − 6 to LUMO + 4, 21.4%, and HOMO − 19 to LUMO + 2, 24.1%) (see Fig. S16D†). One can conclude that even if NCs **1** and **2** bear a similar M_{15}^{+} geometrical configuration, the optical absorption properties are quite different, mainly owing to the differences in the M_1 kernel (Ag *vs.* Au) and M_6 octahedron (Cu *vs.* Au), and probably the subtle difference in the Ag_8 cube as well.

Furthermore, we also calculated the electronic structures of NCs **1** and **2** to unravel the relationship between the electronic structure and the optical absorption properties of M_{15}^{+} NCs. According to the Kohn–Sham (KS) molecular orbital energy level diagram (Fig. 4A and B), there is an obvious energy gap between the HOMO and the remaining occupied orbitals for the two NCs, which may be because the two electrons at the HOMO orbital with higher energy tend to relax to the HOMO – 1 orbital. It is worth noting that for the frontier unoccupied molecular orbitals (including the LUMO), the Ag(sp) atomic orbital makes the most significant contribution in both NCs. That means, for both NCs, Ag_8 cubic atoms are the major contributor to the unoccupied molecular orbitals. It indicates that the unoccupied molecular orbitals of the M_{15}^{+} clusters might be localized at some specific position (*i.e.*, M_8 cube), while the M_1 kernel and M_6 octahedron make less contribution, reminiscent of the case of $M_{21}(SCH_3)_{15}$.[52] This explains that there are triplet peaks located at high wavelength for both NCs. However, for the remaining occupied molecular orbitals (not including the HOMO) particularly the deep occupied orbitals, the Cu(d) atomic orbital makes the most important contribution in NC **1**, while Au(d) and Ag(d) both contributed significantly in NC **2**. For the HOMO, drastic differences can be observed, Ag(sp) and Au(sp) atomic orbitals make the most significant contribution to the HOMO orbital in NCs **1** and **2**, respectively. The absorption band α in NC **1** is primarily attributed to intraband Ag(sp) to Ag(sp) transitions, while the interband Au(d) to Ag(sp) transitions lead to the α band in NC **2**. This finding reveals that the central M(0) atom of M_{15} NCs plays a significant role in the HOMO energy. Moreover, the HOMO energy of NC **1** is higher than that of NC **2**, probably due to the fact that, compared with Ag, the central Au atom has higher cohesive force thus causing NC **2** to have lower HOMO energy than NC **1**. Similarly, band β at 2.22 eV in NC **1** and that at 2.89 eV in NC **2** originate from Ag(sp) to Ag(sp), and Au(d) to Ag(sp) transitions, respectively. Notably, the band γ of NC **1** comprises Cu(d) to Ag(sp) transitions, suggesting that the Cu_6 octahedron is the major contributor to the deep occupied orbitals. The absorption band δ (*i.e.*, 3.63 eV for NC **1** and 3.66 eV for NC **2**) has a large portion of C(p) character of alkynyl ligands, which greatly affects their high-energy absorption bands around ∼350 nm. It can be noted that the same $^{t}BuC{\equiv}C–$ ligand makes almost equal yet predominant contribution to the δ absorption band for both NCs, suggesting the important role of the surface ligand in the optical properties.

Despite the similar structural scaffold of the two NCs, the subtle differences in metal composition and structural coordination mode might result in a vast difference of their stability. The stability of NCs **1** and **2** was investigated by monitoring the time-resolved UV-vis absorbance spectra at different temperatures, in the presence of an oxidant (*e.g.*, H_2O_2) or Lewis base (*e.g.*, CH_3ONa). Fig. 5 shows the intensity of the peaks at 579 nm for NC **1** and 487 nm for NC **2** *versus* time. At room temperature, the absorbance of NCs **1** and **2** remained almost unchanged for 24 h (Fig. S17A and B†), indicating that the two NCs can be stable under ambient conditions. As shown in Fig. 5A, the relative absorbance intensity of NC **2** preserved 81% of its initial value in 24 h, however, NC **1** retained 94%, indicating much less decomposition. It was because both NCs are situated at the lowest energy state, as confirmed by DFT calculations of the vibration frequency of NCs **1** and **2** (Table S10†). When incubated at 60 °C (Fig. 5B), the relative intensity of NC **1** remained 81% at 24 h, slightly higher than that of NC **2** (78%), indicating excellent thermal stability for both NCs. However, the absorption intensity of NC **1** dropped much faster than that of NC **2** in the first 5 h (Fig. S17C and D†), indicating that it is more
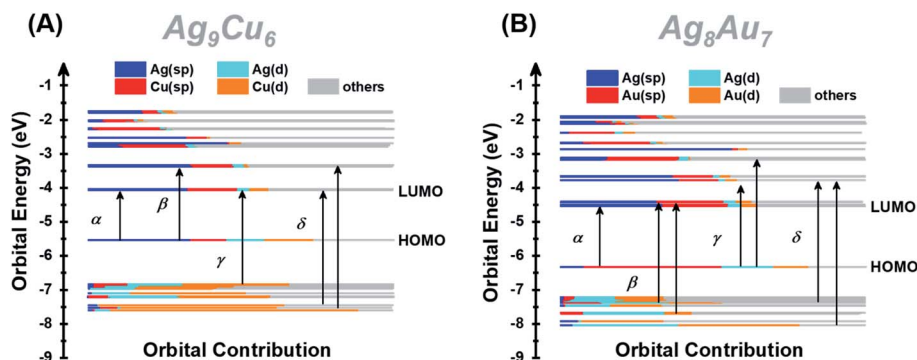

Fig. 4 Kohn–Sham (KS) molecular orbital energy level diagram and the associated populations of atomic orbitals in each K–S molecular orbital for NCs **1** (A) and **2** (B).
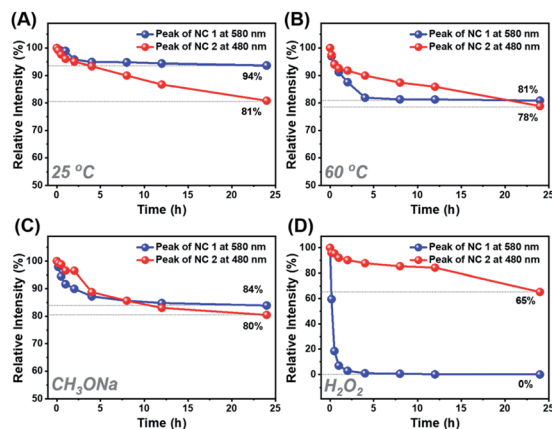
Fig. 5 Stability comparison of NCs **1** and **2** under different conditions. The relative absorption intensity value at specific wavelengths is used (NC **1**, 579 nm; NC **2**, 487 nm) in the time resolved UV-vis absorption spectra. The thermal stability of NCs **1** and **2** in 1,2-dichloroethane solution under (A) ambient conditions and (B) heating to 60 °C. The stability of NCs **1** and **2** in CH_2Cl_2 solution in the presence of (C) an oxidant (H_2O_2) and (D) a Lewis base (CH_3ONa).

susceptible to heat. However, in the following 5–24 h, the relative intensity of NC **1** remained almost unchanged. Previous studies have documented that the thermal stability of bimetallic NCs not only depends on the extent of free electron centralization,[4,53] but also the metal–ligand interaction needs to be considered,[54] specifically, the interaction between the surface metal atoms (Ag, Au or Cu) and the alkynyl ligand must be taken into account for these two title NCs. As shown in Fig. S9,† the σ and π bonds between the metal and carbon atoms of the surface binding motif in NC **1** (Cu1–C1: 1.856 Å; Cu1–C2: 1.884 Å; Ag1–C1: 2.395 Å; Ag2–C2: 2.355 Å) are slightly stronger than those in NC **2** (Au1–C1: 1.983 Å; Au1–C2: 1.980 Å; Ag1–C1: 2.495 Å; Ag2–C2: 2.505 Å). Therefore, the more compact structure of NC **1** can prevent decomposition at higher temperature. Furthermore, NC **1** is more stable than NC **2** in the presence of the Lewis base (1 wt% CH_3ONa in EtOH), but rapidly decomposed upon the addition of the oxidant (30 wt% H_2O_2). As shown in Fig. 5C, NC **1** decomposed slightly faster than NC **2** in the first 5 h, and both reached the same intensity at 8 h, after that, NC **2** decomposed slightly faster. The higher relative intensity (84% *vs.* 80%) indicates that NC **1** possessed slightly superior stability in the presence of the Lewis base. During this process, the color of NC **1** showed no change, while the NC **2** solution gradually turned from orange to light orange, as visualized in Fig. S18A and B.† Note that the cohesive force between Ag and Au in NC **2** is higher than that between Cu and Ag in NC **1**, making NC **2** more vulnerable to the Lewis base, as CH_3ONa is a nucleophilic agent, and hence it can attack the surface of NC **2** more favorably. However, NC **2** is more robust than NC **1** upon adding H_2O_2 aqueous solution (Fig. S18C and D†). As shown in Fig. 5D, NC **1** decomposed completely in 1 h, suggesting that NC **1** is sensitive to H_2O_2, probably because the Cu(ɪ) atoms on the surface of NC **1** can be easily oxidized into Cu(ɪɪ). In contrast, the corresponding Au(ɪ) atoms in NC **2** possessed strong antioxidation capacity. However, it still lost 35% of the initial value, and such

a decomposition can be presumably attributed to the fact that the Ag atoms in the Ag_8 cube are easily attacked by the lone pair electrons of the peroxy radical (O_2^{2-}).[55] Such a phenomenon occurs even more seriously for NC **1**, leading to an accelerated and complete decomposition in 1 h.

Conclusions

In conclusion, a novel homoleptic alkynyl-protected AgCu superatom $[Ag_9Cu_6(^tBuC\equiv C)_{12}]^+$ was synthesized for the first time *via* a one-pot reaction with high yield (>40%). X-ray crystallographic analysis revealed that it possesses a BCC-based $Ag_1@Ag_8@Cu_6$ configuration. Also, the BCC-based $[Au_7Ag_8(^tBuC\equiv C)_{12}]^+$ cluster with a $Au_1@Ag_8@Au_6$ metal core was also prepared by an AGR approach with a ultrahigh yield (>86%). DFT calculations revealed that the different absorption features of the two NCs can be attributed to the differences in the M_1 kernel (Ag *vs.* Au), M_6 octahedron (Cu *vs.* Au), and the subtle differences in the Ag_8 cube. The characteristic absorbance peaks of NCs **1** and **2** are successfully correlated with the specific molecular orbital transitions. NC **1** possessed superior stability to NC **2** at both room temperature and elevated temperature, and NC **1** also showed better tolerance to the Lewis base but is much more sensitive to the oxidant. We envision that this study can stimulate more research efforts on Cu-containing bimetallic superatomic NCs in terms of their synthesis, structural analysis, property exploration and beyond.

Data availability

All the data in this study are provided in the main text and ESI.†

Author contributions

X. M. and Z. T. conceived the idea, X. M. conducted most of the experiments, L. Q., Y. T., and G. M. helped the characterization, L. X. and Y. P. conducted the DFT calculations, X. M. and Z. T. wrote up the draft, Y. P. and Z. T. provided the funding support, and all the authors contributed to the final proof of the manuscript.

Conflicts of interest

There are no conflicts to declare.

Acknowledgements

Notes and references

1 S. Takano and T. Tsukuda, *J. Am. Chem. Soc.*, 2021, **143**, 1683–1698.

2 X. Kang, S. Jin, L. Xiong, X. Wei, M. Zhou, C. Qin, Y. Pei, S. Wang and M. Zhu, *Chem. Sci.*, 2020, **11**, 1691–1697.

3 A. Ghosh, O. F. Mohammed and O. M. Bakr, *Acc. Chem. Res.*, 2018, **51**, 3094–3103.

4 X. Kang, H. Abroshan, S. Wang and M. Zhu, *Inorg. Chem.*, 2019, **58**, 11000–11009.

5 X. Kang, X. Wei, P. Xiang, X. H. Tian, Z. W. Zuo, F. Q. Song, S. X. Wang and M. Z. Zhu, *Chem. Sci.*, 2020, **11**, 4808–4816.

6 S. Wang, X. Meng, A. Das, T. Li, Y. Song, T. Cao, X. Zhu, M. Zhu and R. Jin, *Angew. Chem., Int. Ed.*, 2014, **53**, 2376–2380.

7 M. Suyama, S. Takano and T. Tsukuda, *J. Phys. Chem. C*, 2020, **124**, 23923–23929.

8 X. Zou, S. He, X. Kang, S. Chen, H. Yu, S. Jin, D. Astruc and M. Zhu, *Chem. Sci.*, 2021, **12**, 3660–3667.

9 X. Kang, Y. Li, M. Zhu and R. Jin, *Chem. Soc. Rev.*, 2020, **49**, 6443–6514.

10 Z. Gan, N. Xia and Z. Wu, *Acc. Chem. Res.*, 2018, **51**, 2774–2783.

11 Y. Du, H. Sheng, D. Astruc and M. Zhu, *Chem. Rev.*, 2020, **120**, 526–622.

12 T. Kawawaki, Y. Imai, D. Suzuki, S. Kato, I. Kobayashi, T. Suzuki, R. Kaneko, S. Hossain and Y. Negishi, *Chem.–Eur. J.*, 2020, **26**, 16150–16193.

13 H. Hirai, S. Ito, S. Takano, K. Koyasu and T. Tsukuda, *Chem. Sci.*, 2020, **11**, 12233–12248.

14 S. Wang, Q. Li, X. Kang and M. Zhu, *Acc. Chem. Res.*, 2018, **51**, 2784–2792.

15 A. Ghosh, O. F. Mohammed and O. M. Bakr, *Acc. Chem. Res.*, 2018, **51**, 3094–3103.

16 N. Yan, N. Xia, L. Liao, M. Zhu, F. Jin, R. Jin and Z. Wu, *Sci. Adv.*, 2018, **4**, eaat7259.

17 Y. Li, T. Higaki, X. Du and R. Jin, *Adv. Mater.*, 2020, **32**, e1905488.

18 J. Yang and R. Jin, *ACS Mater. Lett.*, 2019, **1**, 482–489.

19 Q. F. Yao, Z. N. Wu, Z. H. Liu, Y. Z. Lin, X. Yuan and J. P. Xie, *Chem. Sci.*, 2021, **12**, 99–127.

20 J. Yan, H. Su, H. Yang, C. Hu, S. Malola, S. Lin, B. K. Teo, H. Hakkinen and N. Zheng, *J. Am. Chem. Soc.*, 2016, **138**, 12751–12754.

21 S. Yang, J. Chai, H. Chong, Y. Song, H. Yu and M. Zhu, *Chem. Commun.*, 2018, **54**, 4314–4316.

22 Y. Bao, X. Wu, H. Gao, M. Zhou, S. Chen, S. Jin, H. Yu and M. Zhu, *Dalton Trans.*, 2020, **49**, 17164–17168.

23 X. Ma, Y. Tang, G. Ma, L. Qin and Z. Tang, *Nanoscale*, 2021, **13**, 602–614.

24 L. L. Zhang, G. Zhou, G. Zhou, H. K. Lee, N. Zhao, O. V. Prezhdo and T. C. W. Mak, *Chem. Sci.*, 2019, **10**, 10122–10128.

25 P. Maity, S. Takano, S. Yamazoe, T. Wakabayashi and T. Tsukuda, *J. Am. Chem. Soc.*, 2013, **135**, 9450–9457.

26 X. Ma, Z. Tang, L. Qin, J. Peng, L. Li and S. Chen, *Nanoscale*, 2020, **12**, 2980–2986.

27 Z. Lei, X. K. Wan, S. F. Yuan, J. Q. Wang and Q. M. Wang, *Dalton Trans.*, 2017, **46**, 3427–3434.

28 Z. Lei, X. K. Wan, S. F. Yuan, Z. J. Guan and Q. M. Wang, *Acc. Chem. Res.*, 2018, **51**, 2465–2474.

29 X. Ma, G. Ma, L. Qin, G. Chen, S. Chen and Z. Tang, *Sci. China: Chem.*, 2020, **63**, 1777–1784.

30 K. K. Chakrahari, R. P. B. Silalahi, J. H. Liao, S. Kahlal, Y. C. Liu, J. F. Lee, M. H. Chiang, J. Y. Saillard and C. W. Liu, *Chem. Sci.*, 2018, **9**, 6785–6795.

31 T. T. Jia, G. Yang, S. J. Mo, Z. Y. Wang, B. J. Li, W. Ma, Y. X. Guo, X. Chen, X. Zhao, J. Q. Liu and S. Q. Zang, *ACS Nano*, 2019, **13**, 8320–8328.

32 X. K. Wan, J. Q. Wang, Z. A. Nan and Q. M. Wang, *Sci. Adv.*, 2017, **3**, e1701823.

33 X. Y. Chang, G. T. Xu, B. Cao, J. Y. Wang, J. S. Huang and C. M. Che, *Chem. Sci.*, 2017, **8**, 7815–7820.

34 Y. Wang, X. K. Wan, L. Ren, H. Su, G. Li, S. Malola, S. Lin, Z. Tang, H. Hakkinen, B. K. Teo, Q. M. Wang and N. Zheng, *J. Am. Chem. Soc.*, 2016, **138**, 3278–3281.

35 Y. Wang, H. Su, L. Ren, S. Malola, S. Lin, B. K. Teo, H. Hakkinen and N. Zheng, *Angew. Chem., Int. Ed.*, 2016, **55**, 15152–15156.

36 P. Yuan, R. Zhang, E. Selenius, P. Ruan, Y. Yao, Y. Zhou, S. Malola, H. Hakkinen, B. K. Teo, Y. Cao and N. Zheng, *Nat. Commun.*, 2020, **11**, 2229.

37 T. U. Connell, S. Sandanayake, G. N. Khairallah, J. M. White, R. A. O'Hair, P. S. Donnelly and S. J. Williams, *Dalton Trans.*, 2013, **42**, 4903–4907.

38 S. C. K. Hau, M. C. Yeung, V. W. Yam and T. C. W. Mak, *J. Am. Chem. Soc.*, 2016, **138**, 13732–13739.

39 Q. Y. Wang, J. Wang, S. Wang, Z. Y. Wang, M. Cao, C. L. He, J. Q. Yang, S. Q. Zang and T. C. W. Mak, *J. Am. Chem. Soc.*, 2020, **142**, 12010–12014.

40 M. Walter, J. Akola, O. Lopez-Acevedo, P. D. Jadzinsky, G. Calero, C. J. Ackerson, R. L. Whetten, H. Gronbeck and H. Hakkinen, *Proc. Natl. Acad. Sci. U. S. A.*, 2008, **105**, 9157–9162.

41 C. Yin, S. Liu, Z. Qin, Y. Zhang, G. Li and Z. Zhao, *Eur. J. Inorg. Chem.*, 2020, **2021**, 392–397.

42 Z. Qin, S. Sharma, C. Q. Wan, S. Malola, W. W. Xu, H. Hakkinen and G. Li, *Angew. Chem., Int. Ed.*, 2021, **60**, 970–975.

43 H. Shen, Y. Z. Han, Q. Wu, J. Peng, B. K. Teo and N. Zheng, *Small Methods*, 2020, **5**, 2000603.

44 W. Du, S. Jin, L. Xiong, M. Chen, J. Zhang, X. Zou, Y. Pei, S. Wang and M. Zhu, *J. Am. Chem. Soc.*, 2017, **139**, 1618–1624.

45 X. Zou, Y. Li, S. Jin, X. Kang, X. Wei, S. Wang, X. Meng and M. Zhu, *J. Phys. Chem. Lett.*, 2020, **11**, 2272–2276.

46 X. Gao, S. He, C. Zhang, C. Du, X. Chen, W. Xing, S. Chen, A. Clayborne and W. Chen, *Adv. Sci.*, 2016, **3**, 1600126.

47 Z. Tang, D. A. Robinson, N. Bokossa, B. Xu, S. Wang and G. Wang, *J. Am. Chem. Soc.*, 2011, **133**, 16037–16044.

48 Y. Wang, H. Su, C. Xu, G. Li, L. Gell, S. Lin, Z. Tang, H. Hakkinen and N. Zheng, *J. Am. Chem. Soc.*, 2015, **137**, 4324–4327.

49 Z. J. Guan, J. L. Zeng, S. F. Yuan, F. Hu, Y. M. Lin and Q. M. Wang, *Angew. Chem., Int. Ed.*, 2018, **57**, 5703–5707.

50 J. L. Zeng, Z. J. Guan, Y. Du, Z. A. Nan, Y. M. Lin and Q. M. Wang, *J. Am. Chem. Soc.*, 2016, **138**, 7848–7851.

51 P. Liu, W. Han, M. Zheng, W. Li, J. Ren, A. Tlahuice-Flores and W. W. Xu, *J. Phys. Chem. A*, 2021, **125**, 5933–5938.

52 Y. Li, M. G. Taylor, T. Y. Luo, Y. Song, N. L. Rosi, G. Mpourmpakis and R. Jin, *J. Phys. Chem. Lett.*, 2020, **11**, 7307–7312.

53 X. Kang, X. Wei, S. Jin, Q. Yuan, X. Luan, Y. Pei, S. Wang, M. Zhu and R. Jin, *Proc. Natl. Acad. Sci. U. S. A.*, 2019, **116**, 18834–18840.

54 Q. Tang, G. Hu, V. Fung and D. E. Jiang, *Acc. Chem. Res.*, 2018, **51**, 2793–2802.

55 L. Han, P. Xing and B. Jiang, *Org. Lett.*, 2014, **16**, 3428–3431.